Finite Temperature Magnetism in the Triangular Lattice Antiferromagnet $KErTe_2$

Weiwei Liu(刘维维)[1,2†], Zheng Zhang(张政)[2†*], Dayu Yan(闫大禹)[2], Jianshu Li(李建树)[2], Zhitao Zhang(张志涛)[3], Jianting Ji(籍建葶)[2], Feng Jin(金峰)[2], Youguo Shi(石友国)[2], and Qingming Zhang(张清明)[2,4]

[1]*Department of Physics, Renmin University of China, Beijing 100872, China*
[2]*Beijing National Laboratory for Condensed Matter Physics, and Institute of Physics, Chinese Academy of Sciences, Beijing 100190, China*
[3]*Anhui Province Key Laboratory of Condensed Matter Physics at Extreme Conditions, High Magnetic Field Laboratory, Chinese Academy of Sciences, Hefei 230031, China*
[4]*School of Physical Science and Technology, Lanzhou University, Lanzhou 730000, China*

(Received 11 June 2024; accepted manuscript online 16 August 2024)

After the discovery of the $ARECh_2$ (A = alkali or monovalent ions, RE = rare-earth, Ch = chalcogen) triangular lattice quantum spin liquid (QSL) family, a series of its oxide, sulfide, and selenide counterparts has been consistently reported and extensively investigated. While $KErTe_2$ represents the initial synthesized telluride member, preserving its triangular spin lattice, it was anticipated that the substantial tellurium ions could impart more pronounced magnetic attributes and electronic structures to this material class. This study delves into the magnetism of $KErTe_2$ at finite temperatures through magnetization and electron spin resonance (ESR) measurements. Based on the angular momentum $\hat{J}$ after spin-orbit coupling (SOC) and symmetry analysis, we obtain the magnetic effective Hamiltonian to describe the magnetism of Er^{3+} in $R\bar{3}m$ space group. Applying the mean-field approximation to the Hamiltonian, we can simulate the magnetization and magnetic heat capacity of $KErTe_2$ in paramagnetic state and determine the crystalline electric field (CEF) parameters and partial exchange interactions. The relatively narrow energy gaps between the CEF ground state and excited states exert a significant influence on the magnetism. For example, small CEF excitations can result in a significant broadening of the ESR linewidth at 2 K. For the fitted exchange interactions, although the values are small, given a large angular momentum $J = 15/2$ after SOC, they still have a noticeable effect at finite temperatures. Notably, the heat capacity data under different magnetic fields along the c axis direction also roughly match our calculated results, further validating the reliability of our analytical approach. These derived parameters serve as crucial tools for future investigations into the ground state magnetism of $KErTe_2$. The findings presented herein lay a foundation for exploration of the intricate magnetism within the triangular-lattice delafossite family.

DOI: 10.1088/0256-307X/41/9/097503

Rare-earth chalcogenides, denoted as $ARECh_2$ (with A representing alkali or monovalent metals, RE for rare-earth, and Ch encompassing O, S, Se, and Te), have emerged as compelling candidates for quantum spin liquids (QSL).[1–10] These intriguing materials contrast with previous QSL contenders, such as $ZnCu_3(OH)_6Cl_2$,[11] $EtMe_3Sb[Pd(dmit)_2]_2$,[12] and $YbMgGaO_4$,[13–18] in that they not only possess perfect triangular structures but also offer opportunities for doping and element substitution. This dynamic framework proves to be ideal for probing intricate interactions in strongly correlated electronic systems and complex magnetism,[19,20] facilitated by the distinctive electronic properties intrinsic to rare-earth ions. The potency of these materials can be attributed to several factors. Firstly, the robust spin-orbit coupling (SOC) in rare-earth ions engenders formidable magnetic anisotropy. Secondly, certain rare-earth ions, like Er^{3+} and Yb^{3+}, possess Kramer's degeneracy, safeguarded by time-reversal symmetry in their crystalline electric field (CEF) ground state, which is doubly degenerate. Thirdly, the $4f$ electrons of rare-earth ions, in contrast to the $3d$ electrons of transition metal ions, are effectively shielded by outer electrons, leading to diminished CEF excitations bridging the ground and excited states. Notably, these subtle energy gaps profoundly impact the thermodynamic and spectroscopic attributes of the materials, as confirmed through numerous experimental investigations. For instance, the thermodynamic data of $NaYbSe_2$ reveals a distinct characteristic temperature of 25 K,[21] a manifestation of CEF effects. Above this temperature, CEF excitations exert significant influence on both thermodynamic and spectroscopic observations. Furthermore, in the case of $KErSe_2$, which possesses a small CEF energy gap between the ground and first excited states (approximately 1 meV),[20] the magnetization and thermodynamic data are predominantly governed by CEF excitations, even at low temper-

†These authors contributed equally to the work.
*Corresponding author. Email: zhangzheng@iphy.ac.cn
© 2024 Chinese Physical Society and IOP Publishing Ltd

atures.

In a recent achievement, we have successfully synthesized single-crystal samples of $KErTe_2$.[22] This marks an advancement as the premier telluride among rare-earth chalcogenides to undergo comprehensive investigation. $KErTe_2$ is isomorphic to $NaYbCh_2$ (Ch encompassing O, S, Se, and Te), boasting a flawless triangular lattice structure within the $R\bar{3}m$ space group. The central Er^{3+} ion resides in an octahedral coordination, surrounded by six Te^{2-} ligands. Comparatively, $KErTe_2$ deviates slightly from its counterpart $KErSe_2$,[20] with only one element substituted, suggesting similar CEF excitation characteristics for these two compounds. It is noteworthy that the electronegativity of Te^{2-} is comparatively less than that of Se^{2-}, implying that the CEF excitation energy levels in $KErTe_2$ could be even weaker than those in $KErSe_2$. Furthermore, it is important to recognize that $KErTe_2$ displays the narrowest valence band bandwidth (approximately 0.9 eV) within this material family,[22] rendering it an opportune platform for delving into metallization and superconductivity phenomena.[23,24] Hence, the exploration of $KErTe_2$'s physical properties assumes a pivotal relevance, augmenting our understanding of this intriguing material and its potential implications.

In this Letter, we present a comprehensive investigation of $KErTe_2$ magnetism at finite temperatures, including temperature-dependent magnetization (M/H vs T), magnetic field-dependent magnetization (M vs H), magnetic heat capacity, and electron spin resonance (ESR). Firstly, we construct an effective magnetic Hamiltonian based on the angular momentum operator $\hat{J}$ to describe the magnetism of Er^{3+} ions, considering their weak CEF excitations. Furthermore, in order to quantitatively analyze the measured magnetization and magnetic heat capacity data, we apply a mean-field approximation to the effective magnetic Hamiltonian. This provides a satisfactory explanation for the magnetism of $KErTe_2$ in the paramagnetic state at high temperatures. Next, we successfully derive the CEF parameters and angular momentum $\hat{J}$ exchange interactions ϑ_{zz} (~ 0.034 K) and $\vartheta_{\pm}$ (~ 0.001 K) for $KErTe_2$ based on magnetization data. Using these parameters, we are able to effectively simulate the M/H–T and magnetic heat capacity data at finite temperatures, and compute the CEF energy levels and wavefunctions of $KErTe_2$. Intriguingly, our findings reveal that $KErTe_2$ exhibits minuscule CEF excitation energy levels, indicating that the impact of CEF excitations on magnetism cannot be ignored, even at temperatures as low as 2 K. For the angular momentum operator $\hat{J}$ exchange interactions, ϑ_{zz} and $\vartheta_{\pm}$, though numerically small, considering the large value of $J = 15/2$ after SOC, they can still have an impact on magnetism at finite temperatures. Lastly, drawing on the CEF energy levels of $KErTe_2$, we elucidate the origin of the broad linewidth observed in the ESR spectrum at 2 K. Our comprehensive study of $KErTe_2$'s CEF properties lays a solid foundation for future investigations into the material's ground state magnetism at low temperatures. We propose that forthcoming explorations could encompass advanced methodologies, such as thermodynamic measurements at millikelvin levels, inelastic neutron scattering experiments, exact diagonalization (ED), and density matrix renormalization group (DMRG) calculations, to deepen our comprehension of this intriguing material's properties.

Samples and Experimental Techniques. Single crystals of $KErTe_2$, measuring approximately 3 mm, were successfully synthesized utilizing the Te-flux method.[22] The conclusive evidence of a singular high-quality crystal is substantiated through single-crystal imaging and the x-ray diffraction pattern of $KErTe_2$[22,25] (refer to the Supplementary Material for details). These single crystals constituted the basis for our M/H–T, M–H, heat capacity, and ESR experiments. Furthermore, nonmagnetic isostructural $KLuTe_2$ samples (both polycrystalline and single crystal),[22] synthesized using similar methods, were used to simulate the lattice contribution to the heat capacity of $KErTe_2$.

Approximately 5 mg of $KErTe_2$ single crystal was meticulously prepared to facilitate M/H–T and M–H experiments. These anisotropic measurements were conducted using a DynaCool Quantum Design physical property measurement system (PPMS) across a temperature range of 2–300 K, while applying magnetic fields varying from 0 to 10 T. This comprehensive study encompassed measurements both within the ab plane and along the c axis of the singular crystal specimen.

A sample of approximately 5 mg composed of a singular $KErTe_2$ crystal was employed for conducting heat capacity measurements spanning the temperature range of 1.8–20 K. The measurements were conducted under magnetic fields of 0, 1, 2, 4, 6, and 9 T with the PPMS system. Notably, the measurements were focused along the c axis of a single crystal. To simulate the lattice contribution of $KErTe_2$, heat capacity data for a non-magnetic single crystal of $KLuTe_2$ were also acquired using the PPMS system.

ESR measurements were meticulously conducted utilizing a Bruker EMX plus 10/12 continuous-wave spectrometer, operating within X-band frequencies (approximately $f \sim 9.4$ GHz). These measurements were carried out within the ab plane and along the c axis of the $KErTe_2$ crystal, all at a temperature of 2 K.

Electronic Configuration, Er^{3+} Ion Environment, and Effective Magnetic Hamiltonian. The $4f$ orbital of Er^{3+} accommodates 11 electrons, yielding a total spin quantum number S of 3/2. Given that the orbital quantum number L equals 6 and considering the robust SOC exhibited by $4f$ electrons,[26] a spectral term $^4I_{15/2}$ featuring a 16-fold degeneracy and another spectral term $^4I_{13/2}$ with a 14-fold degeneracy emerge. An energy distinction of around 0.8 eV (~ 9000 K) separates these two spectral terms. Consequently, the spectral term $^4I_{15/2}$ denotes the SOC ground state configuration. Furthermore, it is worth acknowledging that the energy scale of CEF excitations within rare-earth ions falls considerably below the 0.8 eV threshold. Consequently, the effect of energy level transitions stemming from SOC can be safely disregarded when assessing CEF excitation and magnetism dynamics.

Considering that the CEF excitations are typically weak in the Er^{3+} ions system, even at several Kelvin, CEF excitations may still contribute to magnetism at low temperatures. Meanwhile, interactions between magnetic ions also gradually play a role in magnetism. Therefore, it is more appropriate to describe the magnetic Hamiltonian between Er^{3+} ions using the angular momentum $\hat{J}$ after SOC. Based on these considerations, we have redefined the effective magnetic Hamiltonian for the Er^{3+} ion system, incorporating CEF, angular momentum $\hat{J}$ exchange interactions, and Zeeman effects. The new Hamiltonian reads[27]

$$H = H_{\mathrm{CEF}} + \sum_{\langle ij \rangle} \vartheta_{ij}^{\alpha,\beta} J_i^{\alpha} J_j^{\beta} - \mu_0 \mu_{\mathrm{B}} g_J \sum_i h_x J_i^x + h_y J_i^y + h_z J_i^z, \tag{1}$$

where the first term represents the CEF Hamiltonian describing the single-site effects of the angular momentum $\hat{J}$, the second term accounts for the exchange interactions Hamiltonian capturing the many body effects of the angular momentum $\hat{J}$, $\vartheta_{ij}^{\alpha,\beta}$ (α, $\beta = x$, y, or z) are the exchange interactions, the final term describes the Zeeman effect on the angular momentum $\hat{J}$ influenced by the magnetic field, g_J is Landé g-factor after SOC, which is 6/5 for Er^{3+}, and h_α ($\alpha = x$, y, z) is the magnetic field.

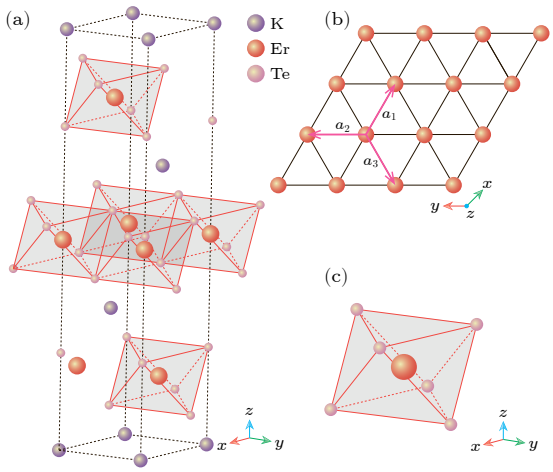

Fig. 1. (a) Crystal structure of $KErTe_2$. (b) Two-dimensional triangular plane formed by Er^{3+} ions. Three directions, a_1, a_2, and a_3, represent the orientations of the phase factor on the anisotropic spin-exchange interaction Hamiltonian, respectively. (c) Octahedral structure with D_{3d} point group symmetry formed by the central Er^{3+} ion and the surrounding 6 Te^{2-} anions.

In $KErTe_2$, possessing the $R\bar{3}m$ space group symmetry [as depicted in Fig. 1(a)], the arrangement entails an octahedral structure wherein the Er^{3+} ion is enveloped by Te^{2-} anions. This structure conforms to a D_{3d} point group configuration [illustrated in Fig. 1(c)]. Therefore, the CEF Hamiltonian can be formally expressed as[9,28]

$$H_{\mathrm{CEF}} = \sum_i B_2^0 O_2^0 + B_4^0 O_4^0 + B_4^3 O_4^3 + B_6^0 O_6^0 + B_6^3 O_6^3 + B_6^6 O_6^6, \tag{2}$$

where B_m^n is the CEF parameter and O_m^n is the Steven operator. Given that Er^{3+} represents a Kramers ion characterized by an odd number of electrons, each state within the CEF is doubly degenerate and is protected by the conservation of time-reversal symmetry. For the triangular lattice, the exchange interactions Hamiltonian for the angular momentum $\hat{J}$ can be further simplified based on symmetry analysis. The interactions along the a_1-bond allow four spatial symmetry operations: one is the C_2 rotational operation along the a_1-bond, another is the C_3 rotational operation along the c axis, and the translations T_1 and T_2 along the a_1-bond and a_2-bond directions, respectively. Considering the C_2 rotational operation along the a_1-bond, y becomes $-y$, and z becomes $-z$. To keep the matrix of interactions invariant under these operations, ϑ_{xy}, ϑ_{xz}, ϑ_{yx}, and ϑ_{zx} must be zero. As a result, the exchange interaction Hamiltonian for the a_1-bond transforms into the following form:

$$H_{a_1-\mathrm{bond}} = \sum_{\langle ij \rangle} \begin{pmatrix} J_i^x & J_i^y & J_i^z \end{pmatrix} \cdot \begin{pmatrix} \vartheta_{xx} & 0 & 0 \\ 0 & \vartheta_{yy} & \vartheta_{yz} \\ 0 & \vartheta_{zy} & \vartheta_{zz} \end{pmatrix} \begin{pmatrix} J_j^x \\ J_j^y \\ J_j^z \end{pmatrix}. \tag{3}$$

Considering T_1 operation along the a_1-bond direction, positions i and j can be interchanged. Hence, in the a_1-bond interactions matrix, $\vartheta_{yz} = \vartheta_{zy}$. Angular momentum $\hat{J}$ vectors are usually represented in terms of the Hermitian Cartesian component operators, $\hat{J}^T = (J^x J^y J^z)$. Occasionally, the non-Hermitian ladder operators $J^+ = J^x + iJ^y$ and $J^- = J^x - iJ^y$ are used. Under the representation of the non-Hermitian ladder operators J^+, J^-, and J^z, we define the interactions between the $J_i^+ J_j^+$ and $J_i^- J_j^-$ as $\vartheta_{\pm}$, between $J_i^+ J_j^-$ and $J_i^- J_j^+$ as $\vartheta_{\pm\pm}$, between $J_i^+ J_j^z$, $J_i^- J_j^z$, $J_i^z J_j^+$, and $J_i^z J_j^-$ as $\vartheta_{z\pm}$, and $J_i^z J_j^z$ as ϑ_{zz}. Thus, interactions along the a_1-bond in Hamiltonian can be expressed as

$$H_{a_1-\mathrm{bond}} = \sum_{\langle ij \rangle} \begin{pmatrix} J_i^x & J_i^y & J_i^z \end{pmatrix} \cdot \begin{pmatrix} 2(\vartheta_{\pm} + \vartheta_{\pm\pm}) & 0 & 0 \\ 0 & 2(\vartheta_{\pm} - \vartheta_{\pm\pm}) & \vartheta_{z\pm} \\ 0 & \vartheta_{z\pm} & \vartheta_{zz} \end{pmatrix} \begin{pmatrix} J_j^x \\ J_j^y \\ J_j^z \end{pmatrix}. \tag{4}$$

Applying a clockwise 120° C_3 operation along the c axis yields the angular momentum $\hat{J}$ interactions along the a_2-bond direction:

$$H_{a_2-\mathrm{bond}} = \sum_{\langle ij \rangle} \begin{pmatrix} J_i^x & J_i^y & J_i^z \end{pmatrix} \cdot \begin{pmatrix} 2\vartheta_{\pm} - \vartheta_{\pm\pm} & \sqrt{3}\vartheta_{\pm\pm} & \frac{\sqrt{3}}{2}\vartheta_{z\pm} \\ \sqrt{3}\vartheta_{\pm\pm} & 2\vartheta_{\pm} + \vartheta_{\pm\pm} & -\frac{1}{2}\vartheta_{z\pm} \\ \frac{\sqrt{3}}{2}\vartheta_{z\pm} & -\frac{1}{2}\vartheta_{z\pm} & \vartheta_{zz} \end{pmatrix} \begin{pmatrix} J_j^x \\ J_j^y \\ J_j^z \end{pmatrix}. \tag{5}$$

Continuing the clockwise rotation by 120° further yields the angular momentum $\hat{J}$ interactions Hamiltonian along

the a_3-bond direction:

$$H_{a_3-\text{bond}} = \sum_{\langle ij \rangle} \begin{pmatrix} J_i^x & J_i^y & J_i^z \end{pmatrix} \cdot \begin{pmatrix} 2\vartheta_\pm - \vartheta_{\pm\pm} & -\sqrt{3}\vartheta_{\pm\pm} & -\frac{\sqrt{3}}{2}\vartheta_{z\pm} \\ -\sqrt{3}\vartheta_{\pm\pm} & 2\vartheta_\pm + \vartheta_{\pm\pm} & -\frac{1}{2}\vartheta_{z\pm} \\ -\frac{\sqrt{3}}{2}\vartheta_{z\pm} & -\frac{1}{2}\vartheta_{z\pm} & \vartheta_{zz} \end{pmatrix} \begin{pmatrix} J_j^x \\ J_j^y \\ J_j^z \end{pmatrix}. \tag{6}$$

Based on the effective magnetic Hamiltonian established for Er^{3+} ions, we can analyze the magnetization and magnetic heat capacity data of $KErTe_2$ at finite temperatures.

If we consider the influence of the magnetic field on the Er^{3+} ions, Zeeman term H_{zeeman} should be incorporated into the effective magnetic Hamiltonian.

$$H_{\text{zeeman}} = -\mu_0\mu_{\text{B}} g_j \sum_i h_x \hat{J}_i^x + h_y \hat{J}_i^y + h_z \hat{J}_i^z, \tag{7}$$

where g_j is Lande g-factor after the SOC, which is 6/5 for Er^{3+}, and h_α ($\alpha = x, y, z$) is the magnetic field along the different directions. Since the magnetic effective Hamiltonian is constructed based on the total angular momentum $J = 15/2$, there is no need to consider the anisotropy of the g-factor.

M/H–T, M–H, and Magnetic Heat Capacity of $KErTe_2$. A thorough comprehension of the CEF excitations and exchange interactions in rare-earth magnetic materials serves as a cornerstone for advancing investigations into low-energy quantum magnetism, particularly within the realm of rare-earth QSL candidate materials. Among the various experimental techniques, inelastic neutron scattering (INS) is widely regarded as the most precise method for discerning CEF excitations and the associated CEF parameters in rare-earth materials. Moreover, the low-energy excitations in INS also contain information about exchange interactions. By analyzing these excitation spectra, exchange interactions can be deduced. In addition to INS, magnetization and magnetic heat capacity measurements also yield valuable insights into the CEF and exchange interactions. Specifically, in the case of $KErTe_2$, the magnetization and heat capacity data under different magnetic fields reveal the response of the system to CEF effects and exchange interactions. By employing the angular momentum $\hat{J}$ magnetic effective Hamiltonian and relevant magnetization and thermodynamic calculation formulas, we can simulate the magnetization and magnetic heat capacity data, and obtain these parameters. The material under investigation in this study, $KErTe_2$, is characterized by several key attributes. Firstly, $KErTe_2$ shares significant similarities with $KErSe_2$. In the case of $KErSe_2$, INS data has revealed an energy gap of approximately 1 meV from the CEF ground state to the first excited state.[20] Considering the weaker electronegativity of Te^{2-} compared to Se^{2-}, it is conceivable that $KErTe_2$ may possess even smaller CEF excitations. A notable example involves $NaYbO_2$, $NaYbS_2$, and $NaYbSe_2$. INS indicates that the CEF first excitation energy levels of these materials are 34.8 meV,[5] 23 meV,[7] and 15.79 meV,[9] respectively. It is clearly evident that as the electronegativity of O, S, and Se decrease, the CEF first excitation energy level also continuously decreases. Secondly, the temperature range of M/H–T measurements is 1.8–300 K, and for heat capacity measurements, it is 1.8–20 K. This range effectively encompasses the magnetic and thermodynamic information related to the CEF excitations of $KErTe_2$. In relation to this, we have measured the heat capacity data of $KLuTe_2$, applying Debye's formula to accurately simulate the lattice heat capacity of $KErTe_2$. Thirdly, the smooth M/H–T data indicate that there are no magnetic phase transitions occurring in $KErTe_2$ within the temperature range of 1.8–300 K. Therefore, by employing mean-field approximation on the effective magnetic Hamiltonian, the magnetism in this paramagnetic state can be well described.

We briefly describe the mean-field Hamiltonian suitable for the paramagnetic state. When the magnetic field is applied along the c axis, the magnetic moment of angular momentum $\hat{J}$ is almost aligned with the direction of the c axis. The contributions of order parameters $\langle J^x \rangle$ and $\langle J^y \rangle$ can be neglected. Thus, the Hamiltonian can be simplified to

$$\begin{aligned} H_{\text{MF-}c\text{-axis}} = & \sum_i B_2^0 O_2^0 + B_4^0 O_4^0 + B_4^3 O_4^3 + B_6^0 O_6^0 \\ & + B_6^3 O_6^3 + B_6^6 O_6^6 + \frac{6\vartheta_\pm M^z}{\mu_0\mu_{\text{B}} g_J} \sum_i J_i^z \\ & - \mu_0\mu_{\text{B}} g_J \sum_i h_z J_i^z. \end{aligned} \tag{8}$$

Similarly, when the magnetic field is in the ab plane, the contribution of the order parameter $\langle J^z \rangle$ is almost zero. The Hamiltonian takes the following form:

$$\begin{aligned} H_{\text{MF-}ab\text{-plane}} = & \sum_i B_2^0 O_2^0 + B_4^0 O_4^0 + B_4^3 O_4^3 + B_6^0 O_6^0 \\ & + B_6^3 O_6^3 + B_6^6 O_6^6 + \frac{12\vartheta_\pm M^x}{\mu_0\mu_{\text{B}} g_J} \sum_i J_i^x \\ & - \mu_0\mu_{\text{B}} g_J \sum_i h_x J_i^x. \end{aligned} \tag{9}$$

Therefore, under the mean-field approximation, the CEF parameters and the diagonal exchange interactions ϑ_{zz} and $\vartheta_\pm$ are retained. For the remaining two off-diagonal interactions $\vartheta_{\pm\pm}$ and $\vartheta_{z\pm}$, the ED or DMRG methods are employed. Meanwhile, thermodynamic or INS data at lower temperatures are required to extract the off-diagonal interactions.

In light of these considerations, a promising avenue emerges: fitting and simulating the magnetization and magnetic heat capacity data of $KErTe_2$ to obtain the CEF parameters and interactions ϑ_{zz} and $\vartheta_\pm$. This approach allows us to gain a comprehensive understanding of the magnetism of $KErTe_2$ at finite temperatures.

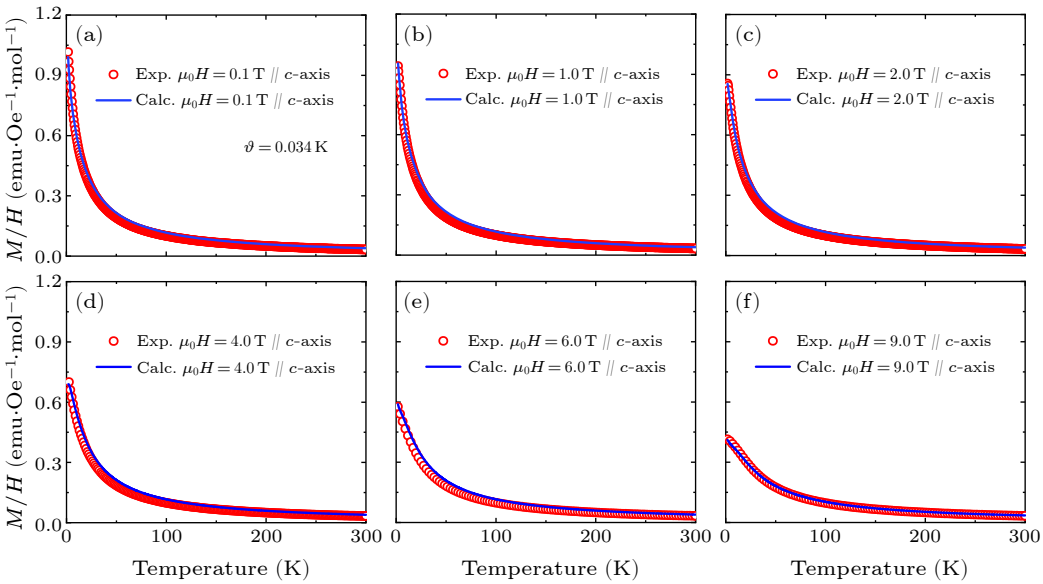

Fig. 2. M/H–T data (open red circles) under different magnetic fields along the c axis of $KErTe_2$ and the simulation results (solid blue lines).

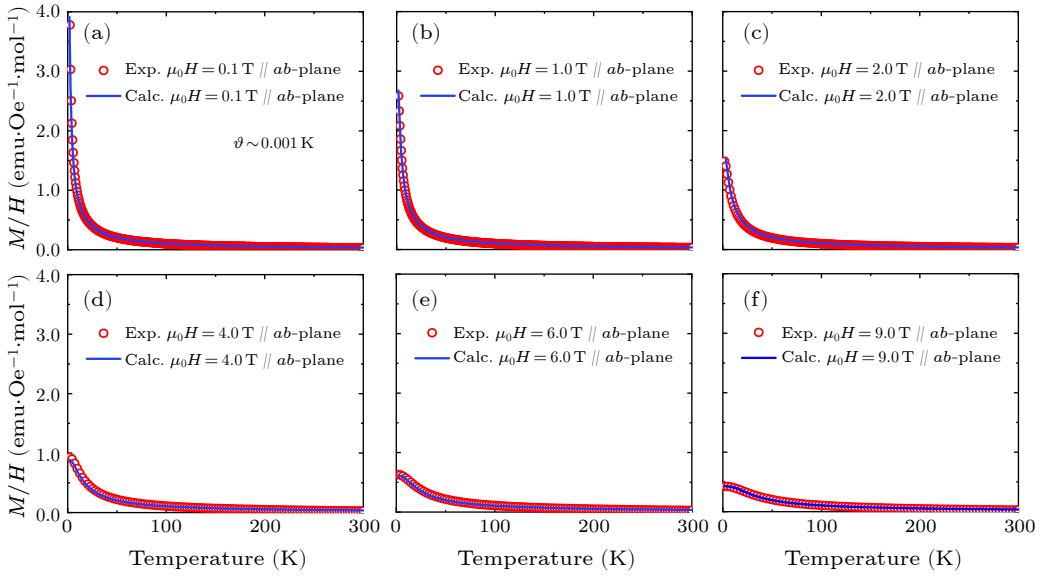

Fig. 3. M/H–T data (open red circles) under different magnetic fields in the ab plane of $KErTe_2$ and the simulation results (solid blue lines).

For the purpose of fitting the CEF parameters and exchange interactions ϑ_{zz} and $\vartheta_{\pm}$, we have opted to utilize the M/H–T data of $KErTe_2$ under a magnetic field 0.1 T. This fitting process encompasses a temperature range spanning from 1.8 K to 300 K. As a starting point for our parameter estimation, we have chosen to employ the CEF parameters obtained from $KErSe_2$ as initial values.[20] The formula used for magnetization calculations to facilitate the CEF parameter and exchange interactions fitting is expressed as

$$\chi_{ab\text{-plane}} = \frac{\mu_B g_j N_A \sum_i \exp(-\frac{E_i}{k_B T})\langle\varphi_i|J_x|\varphi_i\rangle}{h_{ab}\sum_i \exp(-\frac{E_i}{k_B T})}, \quad (10)$$

$$\chi_{c\text{-axis}} = \frac{\mu_B g_j N_A \sum_i \exp(-\frac{E_i}{k_B T})\langle\varphi_i|J_z|\varphi_i\rangle}{h_c\sum_i \exp(-\frac{E_i}{k_B T})}, \quad (11)$$

where h_{ab} and h_c are magnetic fields in the ab plane and along the c axis, respectively. E_i and $|\varphi_i\rangle$ are the energy level and wave function obtained by the diagonalized mean-field Hamiltonian.

Figures 2 and 3 display the M/H–T experimental data of $KErTe_2$ under different magnetic fields, along with the corresponding simulation results. Through the fitting, we obtain the CEF parameters (see Table 1) and $\vartheta_{zz} = 0.034$ K and $\vartheta_{\pm} = 0.001$ K. From the fitting and simulation results, it is evident that the CEF parame-

ters and exchange interactions obtained from our fitting can effectively reproduce the M/H–T data under different magnetic fields, indicating the reasonableness of these parameters. We also calculated the CEF energy levels and wave functions, as listed in Table 2. For the exchange interactions, although the fitted parameters are tiny, considering the large angular momentum of $J = 15/2$ after SOC, they would be amplified by a factor of $\frac{J(J+1)}{S(S+1)} = 85$ compared to the effective $S = 1/2$.[20] Similarly, based on the molecular-field theory, the spin exchange interactions for $KErSe_2$ derived from the fitting magnetization data are $J_{ab} = 0.4(3)\,\mu eV$ ($\sim 0.005\,K$) and $J_c = -2.4(4)\,\mu eV$ ($\sim -0.028\,K$),[20] which are on the same energy scale as the spin exchange interactions of $KErTe_2$.

Table 1. The fitted results of $KErTe_2$ CEF parameters.

B_2^0 (meV)	B_4^0 (meV)	B_4^3 (meV)	B_6^0 (meV)	B_6^3 (meV)	B_6^6 (meV)
-3.070×10^{-2}	-1.942×10^{-2}	-1.050×10^{-2}	1.378×10^{-6}	6.146×10^{-6}	5.536×10^{-5}

Table 2. The CEF energy levels and wave functions of $KErTe_2$.

Energy levels (meV)		CEF wave functions
Ground state	0	$\|\psi^+\rangle = 0.17\|\frac{13}{2}\rangle + 0.29\|\frac{11}{2}\rangle + 0.18\|\frac{7}{2}\rangle + 0.50\|\frac{5}{2}\rangle + 0.03\|\frac{1}{2}\rangle$ $+0.10\|-\frac{1}{2}\rangle - 0.16\|-\frac{5}{2}\rangle - 0.54\|-\frac{7}{2}\rangle + 0.09\|-\frac{11}{2}\rangle + 0.52\|-\frac{13}{2}\rangle$ $\|\psi^-\rangle = 0.52\|\frac{13}{2}\rangle - 0.09\|\frac{11}{2}\rangle + 0.54\|\frac{7}{2}\rangle - 0.16\|\frac{5}{2}\rangle + 0.10\|\frac{1}{2}\rangle$ $-0.03\|-\frac{1}{2}\rangle - 0.50\|-\frac{5}{2}\rangle - 0.18\|-\frac{7}{2}\rangle + 0.29\|-\frac{11}{2}\rangle - 0.17\|-\frac{13}{2}\rangle$
1st excited state	0.49	$\|\psi^+\rangle = 0.02\|\frac{15}{2}\rangle + 0.16\|\frac{9}{2}\rangle + 0.47\|\frac{3}{2}\rangle + 0.17\|-\frac{3}{2}\rangle - 0.54\|-\frac{9}{2}\rangle + 0.65\|-\frac{15}{2}\rangle$ $\|\psi^-\rangle = -0.65\|\frac{15}{2}\rangle - 0.54\|\frac{9}{2}\rangle - 0.17\|\frac{3}{2}\rangle + 0.47\|-\frac{3}{2}\rangle - 0.16\|-\frac{9}{2}\rangle + 0.02\|-\frac{15}{2}\rangle$
2nd excited state	2.72	$\|\psi^+\rangle = 0.09\|\frac{13}{2}\rangle - 0.40\|\frac{11}{2}\rangle - 0.09\|\frac{7}{2}\rangle + 0.07\|\frac{5}{2}\rangle - 0.29\|\frac{1}{2}\rangle$ $+0.78\|-\frac{1}{2}\rangle + 0.03\|-\frac{5}{2}\rangle - 0.23\|-\frac{7}{2}\rangle + 0.15\|-\frac{11}{2}\rangle - 0.24\|-\frac{13}{2}\rangle$ $\|\psi^-\rangle = 0.24\|\frac{13}{2}\rangle + 0.15\|\frac{11}{2}\rangle - 0.23\|\frac{7}{2}\rangle - 0.03\|\frac{5}{2}\rangle - 0.78\|\frac{1}{2}\rangle$ $-0.29\|-\frac{1}{2}\rangle + 0.07\|-\frac{5}{2}\rangle + 0.09\|-\frac{7}{2}\rangle + 0.40\|-\frac{11}{2}\rangle + 0.09\|-\frac{13}{2}\rangle$
3rd excited state	4.62	$\|\psi^+\rangle = 0.45\|\frac{13}{2}\rangle - 0.40\|\frac{11}{2}\rangle + 0.08\|\frac{7}{2}\rangle - 0.36\|\frac{5}{2}\rangle - 0.05\|\frac{1}{2}\rangle$ $-0.05\|-\frac{1}{2}\rangle + 0.33\|-\frac{5}{2}\rangle - 0.08\|-\frac{7}{2}\rangle - 0.37\|-\frac{11}{2}\rangle + 0.49\|-\frac{13}{2}\rangle$ $\|\psi^-\rangle = 0.48\|\frac{13}{2}\rangle + 0.37\|\frac{11}{2}\rangle + 0.08\|\frac{7}{2}\rangle + 0.33\|\frac{5}{2}\rangle - 0.05\|\frac{1}{2}\rangle$ $+0.05\|-\frac{1}{2}\rangle + 0.36\|-\frac{5}{2}\rangle + 0.08\|-\frac{7}{2}\rangle - 0.40\|-\frac{11}{2}\rangle - 0.45\|-\frac{13}{2}\rangle$
4th excited state	4.67	$\|\psi^+\rangle = 0.71\|\frac{15}{2}\rangle - 0.22\|\frac{9}{2}\rangle - 0.32\|\frac{3}{2}\rangle + 0.55\|-\frac{3}{2}\rangle - 0.18\|-\frac{9}{2}\rangle - 0.02\|-\frac{15}{2}\rangle$ $\|\psi^-\rangle = -0.02\|\frac{15}{2}\rangle + 0.18\|\frac{9}{2}\rangle + 0.55\|\frac{3}{2}\rangle + 0.32\|-\frac{3}{2}\rangle - 0.22\|-\frac{9}{2}\rangle - 0.71\|-\frac{15}{2}\rangle$
5th excited state	18.43	$\|\psi^+\rangle = 0.29\|\frac{13}{2}\rangle - 0.26\|\frac{11}{2}\rangle - 0.35\|\frac{7}{2}\rangle + 0.16\|\frac{5}{2}\rangle + 0.48\|\frac{1}{2}\rangle$ $-0.25\|-\frac{1}{2}\rangle + 0.31\|-\frac{5}{2}\rangle - 0.18\|-\frac{7}{2}\rangle + 0.50\|-\frac{11}{2}\rangle - 0.15\|-\frac{13}{2}\rangle$ $\|\psi^-\rangle = -0.15\|\frac{13}{2}\rangle - 0.50\|\frac{11}{2}\rangle + 0.18\|\frac{7}{2}\rangle + 0.31\|\frac{5}{2}\rangle - 0.25\|\frac{1}{2}\rangle$ $-0.48\|-\frac{1}{2}\rangle - 0.16\|-\frac{5}{2}\rangle - 0.35\|-\frac{7}{2}\rangle - 0.26\|-\frac{11}{2}\rangle - 0.29\|-\frac{13}{2}\rangle$
6th excited state	20.23	$\|\psi^+\rangle = -0.26\|-\frac{15}{2}\rangle + 0.77\|-\frac{9}{2}\rangle - 0.48\|-\frac{3}{2}\rangle + 0.32\|\frac{3}{2}\rangle - 0.10\|\frac{9}{2}\rangle$ $\|\psi^-\rangle = 0.10\|-\frac{9}{2}\rangle + 0.32\|-\frac{3}{2}\rangle + 0.48\|\frac{3}{2}\rangle + 0.77\|\frac{9}{2}\rangle + 0.26\|\frac{15}{2}\rangle$
7th excited state	21.43	$\|\psi^+\rangle = 0.06\|\frac{13}{2}\rangle + 0.32\|\frac{11}{2}\rangle - 0.14\|\frac{7}{2}\rangle - 0.58\|\frac{5}{2}\rangle + 0.01\|\frac{1}{2}\rangle$ $-0.07\|-\frac{1}{2}\rangle - 0.13\|-\frac{5}{2}\rangle - 0.66\|-\frac{7}{2}\rangle - 0.07\|-\frac{11}{2}\rangle - 0.28\|-\frac{13}{2}\rangle$ $\|\psi^-\rangle = -0.28\|\frac{13}{2}\rangle + 0.07\|\frac{11}{2}\rangle + 0.66\|\frac{7}{2}\rangle - 0.13\|\frac{5}{2}\rangle - 0.07\|\frac{1}{2}\rangle$ $-0.01\|-\frac{1}{2}\rangle + 0.58\|-\frac{5}{2}\rangle - 0.14\|-\frac{7}{2}\rangle + 0.32\|-\frac{11}{2}\rangle - 0.06\|-\frac{13}{2}\rangle$

Basically, heat capacity reflects the energy spectrum of microscopic states. Therefore, magnetic heat capacity can be used to study the magnetic excitation information present at finite temperatures. The thermodynamic calculation formula to calculate magnetic heat capacity is given as follows:

$$C_{\rm mag} = \frac{1}{k_{\rm B}T^2}\frac{\partial}{\partial\beta}\Big(\frac{1}{Z}\frac{\partial Z}{\partial\beta}\Big) = \frac{1}{k_{\rm B}T^2}\Big(\frac{1}{Z}\sum_n E_n^2 {\rm e}^{-\beta E_n} - \Big[\frac{1}{Z}\sum_n E_n {\rm e}^{-\beta E_n}\Big]^2\Big), \quad (12)$$

where Z is the partition function. Similarly, we calculated the magnetic heat capacity data under different magnetic fields based on the mean-field Hamiltonian and compared them with the experimental results, as shown in Fig. 4. Our simulated results are in good agreement with the experimental measurements, especially in the high-temperature and high-magnetic-field ranges. Meanwhile, we can put forward the following discussion:

(I) We use the heat capacity of the non-magnetic reference sample of $KLuTe_2$ to simulate the lattice contribution to the heat capacity of $KErTe_2$, as shown in Fig. 4(a). When the temperature is below 20 K, the heat capacity of $KLuTe_2$ can be well fitted by the Debye formula. By subtracting the lattice heat capacity contribution, we obtain the magnetic heat capacity data of $KErTe_2$ under different magnetic fields along the c axis. For the magnetic heat capacity data under the magnetic field range of 0 to 2 T, we observed a distinct broad peak within the temperature range of 1.8 to 5 K, and with the increasing magnetic field, the magnetic heat capacity contribution within this temperature range significantly increases. This is primarily attributed to the combined effect of low-energy CEF excitations and angular momentum $\hat{J}$ exchange interactions. Furthermore, the energy levels of these doubly degenerate CEF can be released by magnetic fields, allowing for the release of more magnetic entropy. Therefore, we observe a significant enhancement of this broad heat capacity peak.

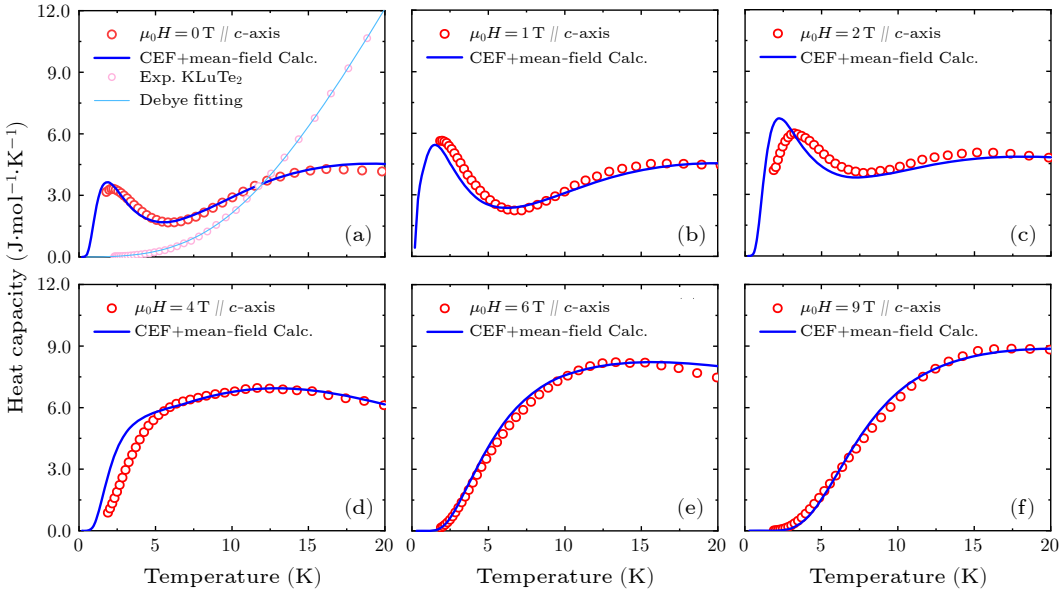

Fig. 4. The red open circles represent experimental results of the magnetic heat capacity under different magnetic fields. The solid blue lines are the simulation results based on the CEF and mean-field theory. Inset: the heat capacity of the non-magnetic reference sample of $KLuTe_2$. The light red open circles are the experimental data, while the light blue solid line is the fitting results based on the Debye formula.

Table 3. The CEF energy levels of $KErTe_2$ and $KErSe_2$. [20]

	CEF0 (meV)	CEF1 (meV)	CEF2 (meV)	CEF3 (meV)	CEF4 (meV)	CEF5 (meV)	CEF6 (meV)	CEF7 (meV)
$KErTe_2$	0	0.49	2.72	4.62	4.67	18.43	20.23	21.43
$KErSe_2$	0	0.903	3.491	5.134	5.538	23.3	25.2	25.4

(II) After the magnetic field exceeds 4 T, the magnetic heat capacity becomes smoother in the temperature range of 1.8–20 K. The main reason for this is that the magnetic moments of the magnetic system have already saturated after 4 T. As shown in Fig. 5, the magnetic system enters a state of magnetic moment saturation after approximately 2 T.

(III) Through comparison between simulated results and experimental data, we find that under high-temperature and high magnetic field conditions, the calculated results agree with the experimental data. However, discrepancies between the calculated results and experimental data exist in the low-temperature and weak-field range. This is because heat capacity describes the microstates, and as the temperature decrease, the off-diagonal interactions between angular momentum $\hat{J}$ and quantum fluctuations become more significant. The mean-field approximation we used only retains the diagonal interactions, hence it is insufficient to describe the microstates at low temperatures.

(IV) We also compare the CEF energy levels of $KErTe_2$ and $KErSe_2$. [20] In Table 3, we can clearly see that CEF excitations in $KErTe_2$ are overall weaker than those in $KErSe_2$. This corresponds with the observation that the intensity of CEF excitations diminishes as the electronegativity of the coordinating anions decreases.

Furthermore, let us briefly discuss the magnetic anisotropy of $KErTe_2$. The magnetic anisotropy is par-

ticularly pronounced at 0.1 T and gradually diminishes as the magnetic field increases. This phenomenon becomes more evident when examining the magnetization data at 2 K (see Fig. 5). We notice that the magnetic moment saturates after approximately 2 T. The ratio of the magnetic moment within the *ab* plane to that along the *c* axis stands at approximately 1.2 : 1. Ignoring the van Vleck paramagnetism contributed by the CEF, the ratio can be used to discuss the magnetic anisotropy of $KErTe_2$. Compared with the ratio of 1.4 : 1 in $KErSe_2$,[20] the magnetic anisotropy of $KErTe_2$ is weaker. This implies that chalcogenide anions can affect the magnetic anisotropy. Similar phenomena are also observed in other compounds, such as $NaYbS_2$ [29] and $NaYbSe_2$,[9,30] where Yb^{3+} serves as the magnetic ion.

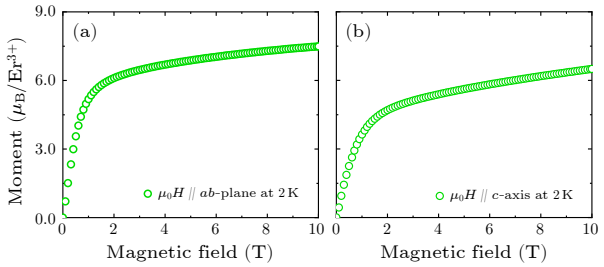

Fig. 5. (a) M–H data of the magnetic field in the *ab* plane at 2 K. (b) M–H data of the magnetic field along the *c* axis at 2 K.

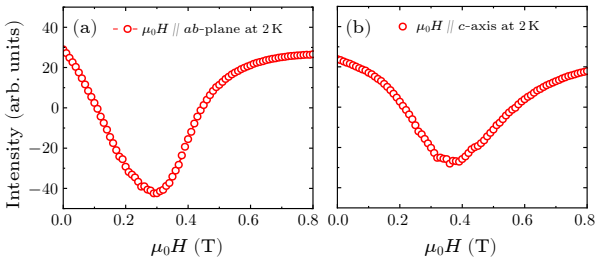

Fig. 6. (a) ESR spectrum in the *ab* plane at 2 K (b) ESR spectrum along the *c* axis at 2 K.

ESR Spectrum of $KErTe_2$. We also conducted ESR spectroscopy measurements on $KErTe_2$ both in the *ab* plane and along the *c* axis at a temperature of 2 K, as depicted in Fig. 6. The ESR spectra, whether in *ab* plane or along the *c* axis, exhibit several broad linewidths. The linewidth of ESR is related to the energy gap between the ground state and excited state of CEF. The relationship between ESR linewidth and CEF energy gap is semi-quantitatively described by the following formula:[9,30]

$$\mu_0 \Delta H \simeq \frac{1}{\exp(\Delta E/T) - 1}, \tag{13}$$

where μ_0 is vacuum permeability, ΔH is the full width at half maximum (FWHM), ΔE is the energy gap from the ground state of CEF to the 1st excited state, and T is the temperature.

From this formula, we can see that when the CEF energy gap is smaller at a fixed temperature, the linewidth of the measured ESR is wider. For some rare-earth chalcogenides with larger CEF energy gaps, such as $NaYbS_2$ [29] and $NaYbSe_2$,[21] we can observe a narrow linewidth in the ESR spectra at low temperatures. For $KErTe_2$, the CEF energy gap obtained from fitting the magnetization data is approximately 0.49 meV, which is much smaller than the gaps of $NaYbS_2$ and $NaYbSe_2$. Therefore, we can observe a significantly broader linewidth in the ESR spectra of $KErTe_2$ that exceeds the measurement range of the instrument. Due to this broader linewidth, the X-band ($\sim$ 9.4 GHz) ESR spectrometer cannot observe a complete ESR spectrum, thereby making it difficult to accurately determine the Landé g-factors at low temperatures. In the future, with high-frequency and high-field ESR spectrometers, we can analyze the CEF excitations and magnetic anisotropy of Er^{3+} ions more accurately.

In summary, we have derived the magnetic effective Hamiltonian to describe the magnetism of Er^{3+} in $KErTe_2$ based on the angular momentum $\hat{J}$ after SOC and symmetry analysis. The effective Hamiltonian comprises terms of the CEF, interactions of the angular momentum $\hat{J}$, and the Zeeman splitting term. By applying the mean-field approximation, we can effectively simplify the magnetic effective Hamiltonian that involves two-body operators. The mean-field Hamiltonian is applicable for the analysis of the paramagnetic state at finite temperatures. Therefore, we have successfully simulated the magnetization and heat capacity data of $KErTe_2$ under different magnetic fields and obtained the CEF parameters and partial angular momentum $\hat{J}$ exchange interactions. Simultaneously, using these fitted CEF parameters, we conducted calculations to determine the CEF energy levels and wave functions of $KErTe_2$. Our findings revealed a relatively small energy gap between the CEF ground state and the first excited state of $KErTe_2$. This feature can well explain a broad linewidth generated in the ESR spectra. We also discussed the magnetic anisotropy in $KErTe_2$, where the Te^{2-} anions would affect the magnetic anisotropy. In a word, our utilization of the CEF theory and mean-field theory has enabled us to comprehensively explore and elucidate the magnetism of $KErTe_2$ at finite temperatures.

Acknowledgments. This work was supported by the National Science Foundation of China (Grant Nos. U1932215 and 12274186), the National Key Research and Development Program of China (Grant No. 2022YFA1402704), the Strategic Priority Research Program of the Chinese Academy of Sciences (Grant No. XDB33010100), and the Synergetic Extreme Condition User Facility (SECUF). A portion of this work was performed at the Steady High Magnetic Field Facilities, High Magnetic Field Laboratory, CAS.

References

[1] Anderson P W 1973 *Mater. Res. Bull.* **8** 153
[2] Anderson P W 1987 *Science* **235** 1196
[3] Liu W W, Zhang Z, Ji J T, Liu Y X, Li J S, Wang X Q, Lei H C, Chen G, and Zhang Q M 2018 *Chin. Phys. Lett.* **35** 117501
[4] Bordelon M M, Kenney E, Liu C X, Hogan T, Posthuma L, Kavand M, Lyu Y Q, Sherwin M, Butch N P, Brown C, Graf M J, Balents L, and Wilson S D 2019 *Nat. Phys.* **15** 1058

[5] Ding L, Manuel P, Bachus S, Grußler F, Gegenwart P, Singleton J, Johnson R D, Walker H C, Adroja D T, Hillier A D, and Tsirlin A A 2019 *Phys. Rev. B* **100** 144432

[6] Ranjith K M, Dmytriieva D, Khim S, Sichelschmidt J, Luther S, Ehlers D, Yasuoka H, Wosnitza J, Tsirlin A A, Kühne H, and Baenitz M 2019 *Phys. Rev. B* **99** 180401

[7] Baenitz M, Schlender P, Sichelschmidt J, Onykiienko Y A, Zangeneh Z, Ranjith K M, Sarkar R, Hozoi L, Walker H C, Orain J C, Yasuoka H, van den Brink J, Klauss H H, Inosov D S, and Doert T 2018 *Phys. Rev. B* **98** 220409

[8] Sarkar R, Schlender P, Grinenko V, Haeussler E, Baker P J, Doert T, and Klauss H H 2019 *Phys. Rev. B* **100** 241116

[9] Zhang Z, Ma X L, Li J S, Wang G H, Adroja D T, Perring T P, Liu W W, Jin F, Ji J T, Wang Y M, Kamiya Y, Wang X Q, Ma J, and Zhang Q M 2021 *Phys. Rev. B* **103** 035144

[10] Ranjith K M, Luther S, Reimann T, Schmidt B, Schlender P, Sichelschmidt J, Yasuoka H, Strydom A M, Skourski Y, Wosnitza J, Kühne H, Doert T, and Baenitz M 2019 *Phys. Rev. B* **100** 224417

[11] Helton J S, Matan K, Shores M P, Nytko E A, Bartlett B M, Yoshida Y, Takano Y, Suslov A, Qiu Y, Chung J H, Nocera D G, and Lee Y S 2007 *Phys. Rev. Lett.* **98** 107204

[12] Itou T, Oyamada A, Maegawa S, Tamura M, and Kato R 2008 *Phys. Rev. B* **77** 104413

[13] Li Y S, Liao H J, Zhang Z, Li S Y, Jin F, Ling L S, Zhang L, Zou Y M, Pi L, Yang Z R, Wang J F, Wu Z H, and Zhang Q M 2015 *Sci. Rep.* **5** 16419

[14] Li Y S, Chen G, Tong W, Pi L, Liu J J, Yang Z R, Wang X Q, and Zhang Q M 2015 *Phys. Rev. Lett.* **115** 167203

[15] Li Y S, Adroja D, Biswas P K, Baker P J, Zhang Q, Liu J J, Tsirlin A A, Gegenwart P, and Zhang Q M 2016 *Phys. Rev. Lett.* **117** 097201

[16] Xu Y, Zhang J, Li Y S, Yu Y J, Hong X C, Zhang Q M, and Li S Y 2016 *Phys. Rev. Lett.* **117** 267202

[17] Shen Y, Li Y D, Wo H L, Li Y S, Shen S D, Pan B Y, Wang Q S, Walker H C, Steffens P, Boehm M, Hao Y Q, Quintero-Castro D L, Harriger L W, Frontzek M D, Hao L J, Meng S Q, Zhang Q M, Chen G, and Zhao J 2016 *Nature* **540** 559

[18] Paddison J A M, Daum M, Dun Z L, Ehlers G, Liu Y H, Stone Matthew?B, Zhou H D, and Mourigal M 2017 *Nat. Phys.* **13** 117

[19] Xing J, Sanjeewa L D, Kim J, Meier W R, May A F, Zheng Q, Custelcean R, Stewart G R, and Sefat A S 2019 *Phys. Rev. Mater.* **3** 114413

[20] Scheie A, Garlea V O, Sanjeewa L D, Xing J, and Sefat A S 2020 *Phys. Rev. B* **101** 144432

[21] Zhang Z, Li J S, Liu W W, Zhang Z T, Ji J T, Jin F, Chen R, Wang J F, Wang X Q, Ma J, and Zhang Q M 2021 *Phys. Rev. B* **103** 184419

[22] Liu W W, Yan D Y, Zhang Z, Ji J T, Shi Y G, Jin F, and Zhang Q M 2021 *Chin. Phys. B* **30** 107504

[23] Zhang Z, Yin Y Y, Ma X L, Liu W W, Li J S, Jin F, Ji J T, Wang Y M, Wang X Q, Yu X H, and Zhang Q M 2020 arXiv:2003.11479 [cond-mat.supr-con]

[24] Jia Y T, Gong C S, Liu Y X, Zhao J F, Dong C, Dai G Y, Li X D, Lei H C, Yu R Z, Zhang G M, and Jin C Q 2020 *Chin. Phys. Lett.* **37** 097404

[25] Supplementary Information

[26] Li Y D, Wang X Q, and Chen G 2016 *Phys. Rev. B* **94** 035107

[27] Schmidt B, Sichelschmidt J, Ranjith K M, Doert T, and Baenitz M 2021 *Phys. Rev. B* **103** 214445

[28] Li Y S, Adroja D, Bewley R I, Voneshen D, Tsirlin A A, Gegenwart P, and Zhang Q M 2017 *Phys. Rev. Lett.* **118** 107202

[29] Sichelschmidt J, Schlender P, Schmidt B, Baenitz M, and Doert T 2019 *J. Phys.: Condens. Matter* **31** 205601

[30] Sichelschmidt J, Schmidt B, Schlender P, Khim S, Doert T, and Baenitz M 2020 *JPS Conf. Proc.* **30** 011096